nature physics

LETTERS

https://doi.org/10.1038/s41567-020-0855-3

Check for updates

A quantum network node with crossed optical fibre cavities

Manuel Brekenfeld[1]✉, Dominik Niemietz[1], Joseph Dale Christesen[1,2] and Gerhard Rempe[1]

Quantum networks provide unique possibilities for resolving open questions on entanglement[1] and promise innovative applications ranging from secure communication to scalable computation[2]. Although two quantum nodes coupled by a single channel are adequate for basic quantum communication tasks between two parties[3], fully functional large-scale quantum networks require a web-like architecture with multiply connected nodes[4]. Efficient interfaces between network nodes and channels can be implemented with optical cavities[5]. Using two optical fibre cavities coupled to one atom, we here realize a quantum network node that connects to two quantum channels, one provided by each cavity. It functions as a passive, heralded and high-fidelity quantum memory that requires neither amplitude- and phase-critical control fields[6–8] nor error-prone feedback loops[9]. Our node is robust, fits naturally into larger fibre-based networks and has prospects for extensions including qubit-controlled quantum switches[10,11], routers[12,13] and repeaters[14,15].

A node in a quantum network must feature several capabilities: it must be equipped with efficient interfaces to quantum channels for connection to neighbouring nodes, it must allow for integration into a larger network with many nodes and many channels and—as a core requirement for its internal functionality—it must serve as a quantum memory that receives, stores and releases an unknown and potentially entangled quantum state better than any classical memory. The simultaneous connection of a node to more than one quantum channel, as reported here, extends the capabilities of the node. Most prominently, it eases the realization of qubit-controlled switches[10,11] and routers[12,13], provides an additional control channel for qubit manipulation, facilitates efficient extraction of information from the node, and extends the set of possible network geometries, including the grid-like structure with end and middle nodes that is visualized in Fig. 1.

Research along these lines has already made significant progress. Most importantly, quantum memories have been implemented in various physical systems ranging from atoms to solids, and from ensembles to single emitters[16–19]. However, it is still a challenge to overcome the losses resulting either from qubit carrier conversion inefficiencies or loss of the photon on its way between nodes, the latter being particularly relevant for long-distance quantum networks.

The effect of losses and finite efficiencies can be remedied in part with a herald that indicates the successful completion of a quantum information-processing protocol[14,20]. Although several schemes for combining quantum memories with heralds have been proposed and investigated[21–27], an advantage over a classical memory could be shown only in a few cases[9,28]. One class of realizations is based on quantum teleportation of a photonic qubit into a quantum memory, where the photonic Bell state measurement of the teleportation protocol provides the herald for successful storage[28]. However, this scheme faces a fundamental efficiency limit of 50% and requires two indistinguishable photons, which is a significant challenge for any practical implementation. A new class arises when the quantum memory is coupled to an optical cavity. This enables the heralded storage of a photonic qubit in a single atom by reflection of a photon from the cavity[9]. However, that memory is limited by two fundamental aspects of the protocol. First, the scheme requires active feedback onto the spin of the atom conditioned on the detection of the reflected photon, leading to extra experimental steps in the protocol that are prone to errors. Second, the detection of the reflected photon from the cavity only heralds the presence of a photon and not successful storage. Successful storage requires a well-prepared atom and perfect coupling between the incoming photon and the cavity mode, neither of which is guaranteed. Accordingly, a storage fidelity comparable to that of other storage schemes, such as those based on stimulated Raman adiabatic passage (STIRAP) without a herald[7], could not be achieved.

By using a novel experimental apparatus, we demonstrate a scheme that overcomes these limitations, realizing a passive, heralded and high-fidelity quantum memory that couples to two quantum channels and can thus serve as a middle node of a quantum network. Our scheme can be motivated from different perspectives. One view is based on the concept of impedance matching[29]. Depending on the exact protocol, a photon impinging onto a cavity can only be stored efficiently if it is not reflected from the input mirror. This is the case when all other losses inside the cavity equal the transmission of the input mirror. For single-sided cavities, this requires additional losses, which have to be induced by the atom in the course of the storage process. In the case of STIRAP-based storage schemes, this is accomplished with suitably timed control fields. In our case, it is achieved in a completely passive manner via vacuum-stimulated Raman scattering into the mode of a second cavity. Detection of a photon at the output of that cavity heralds successful storage. Another view on our memory scheme follows the concept of vacuum-induced transparency[23]. Here, the vacuum field of an optical cavity aligned perpendicular to the propagation direction of an incoming light pulse makes the otherwise absorbing atomic medium transparent. This is accompanied by light scattering into the cavity. Absorption happens when the scattered light escapes from the cavity, thus heralding successful storage. By adding another cavity along the propagation direction of the incoming light, we bring this approach to the quantum regime, making the memory suitable for operation at the single atom and single photon level.

The heart of our apparatus comprises two single-sided fibre Fabry–Pérot cavities[30], based on CO_2-laser-machined mirrors, crossing each other at an angle of 90° (Fig. 1a). We refer to the cavity through which photonic qubits enter and exit the system as the

[1]Max-Planck-Institut für Quantenoptik, Garching, Germany. [2]Present address: National Institute of Standards and Technology, Boulder, CO, USA.
✉e-mail: manuel.brekenfeld@mpq.mpg.de

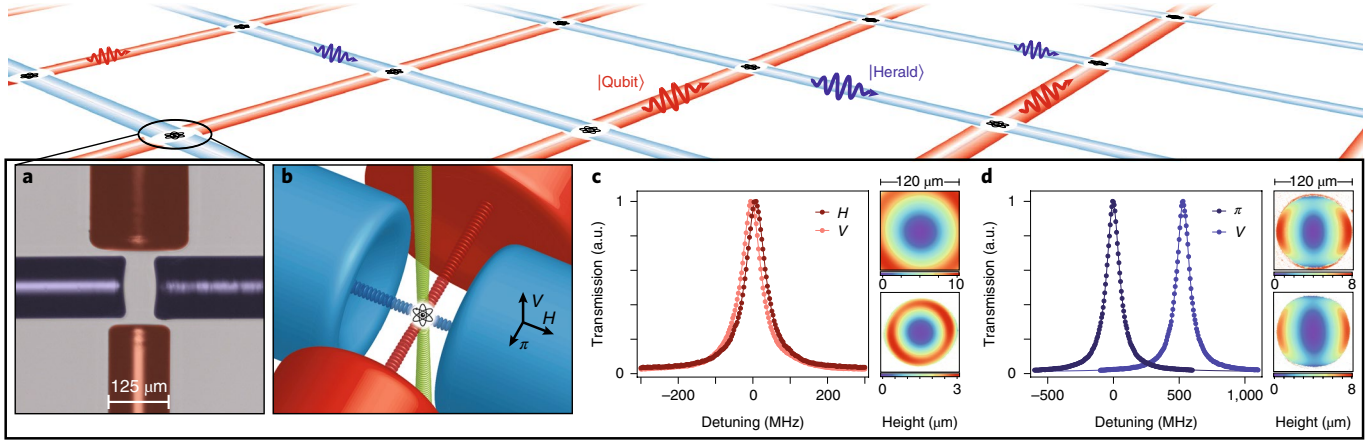

Fig. 1 | Crossed optical fibre cavities. The top of the figure is an artist's view of a grid-like quantum network based on crossed fibre cavities. **a**, Coloured photograph of a quantum node. Red, qubit cavity; blue, herald cavity. **b**, Schematic of the crossed fibre cavities. The coloured intersecting beams illustrate the three-dimensional (3D) optical lattice, which is used to trap a single atom (shown in black) at the crossing point of the cavity modes. **c**,**d**, Transmission spectra of the empty fibre cavities, as well as height maps of their constituting fibre tip surfaces, for the qubit cavity (**c**) and the herald cavity (**d**). Spectra in different colours represent different input polarizations, which are chosen along the eigenpolarizations of the cavities. The strongly elliptical mirror surfaces of the herald cavity lead to a large frequency splitting of the polarization eigenmodes. Statistical error bars are smaller than the data points. Solid lines are Lorentzian fits to the data.

qubit cavity (shown in red in Fig. 1a). The qubit cavity has spherical mirror surfaces to ensure polarization-independent resonance frequencies (Fig. 1c), and left-circular (L) and right-circular (R) polarizations are used as the polarization basis for the qubit cavity, whose symmetry axis defines the quantization axis throughout this Letter. The cavity shown in blue in Fig. 1a is used to create and collect herald photons during the storage process, and we refer to it in the following as the herald cavity. It was intentionally fabricated with strongly elliptical mirror surfaces, leading to two non-degenerate linear polarization eigenmodes[31] (Fig. 1d), one of which is aligned to coincide with the π-polarization of our system. This allows us to selectively couple the herald cavity to atomic transitions exclusively with the π-polarization, which is orthogonal to the qubit cavity polarizations. We emphasise that, even though the frequency splitting of polarization eigenmodes is large, the herald cavity provides coupling to a fully fledged quantum channel and is perfectly suitable for operation with polarization qubits in other protocols[32].

Single ^{87}Rb atoms are trapped at the crossing point of the cavity modes inside a 3D optical lattice (Fig. 1b; see Methods for details). Depending on the atomic transition, both cavities show strong atom–photon coupling (Supplementary Fig. 1).

We operate the heralded quantum memory on the D_2 line of rubidium ($5^2S_{1/2} \leftrightarrow 5^2P_{3/2}$, 780 nm) with the qubit cavity locked to the $F = 1 \leftrightarrow F' = 2$ transition and the π-polarization mode of the herald cavity locked to the $F = 2 \leftrightarrow F' = 2$ transition (Fig. 2a). To characterize the memory, we use weak coherent laser pulses containing $\overline{n} \approx 0.5$ photons on average as our photonic qubit input states, where the polarization is used to encode the input qubit $|\psi_{\mathrm{in}}\rangle = \alpha|R\rangle + \beta|L\rangle$. The experiment starts by optically pumping the atom to the $|F = 1, m_F = 0\rangle$ initial state and subsequently sending a photonic qubit into the qubit cavity. This leads, ideally, to vacuum-stimulated emission of a photon into the herald cavity and the simultaneous transition of the atom to a final state where the qubit is encoded in a superposition of Zeeman states:

$$(\alpha|R\rangle + \beta|L\rangle)_{\mathrm{Input}}|F = 1, m_F = 0\rangle_{\mathrm{Atom}} \rightarrow$$
$$(\alpha|F = 2, m_F = +1\rangle + \beta|F = 2, m_F = -1\rangle)_{\mathrm{Atom}}|1\rangle_{\mathrm{Herald}}$$

Due to the strong birefringence, only the desired π-polarized decay is enhanced by the herald cavity. Detection of the emitted photon heralds successful storage and, after some variable storage time, the atomic state is read out again. To that end, a π-polarized laser pulse ($\overline{n} \approx 6$) is sent onto the herald cavity, which inverts the write process and leads to the emission of a photon into the qubit cavity. The polarization of this re-emitted photon is then analysed.

Figure 3a shows the result of a characterization of our memory using state tomography of the readout polarization states for all six input polarizations along the coordinate axes of the Poincaré sphere with an effective storage time of 1.1 μs. Using post-selection on events where a herald photon was detected during the preceding write pulse, we find an average state fidelity $\overline{\mathcal{F}}_{\mathrm{s}}$ of 94.7 ± 0.2%, far beyond the classical limit of 69% for the applied coherent input. Alternatively, an underlying quantum process can be deduced from the data using a maximum-likelihood fit, leading to a process fidelity $\mathcal{F}_{\mathrm{p}}$ of 92.2 ± 0.3%, in perfect agreement with the average state fidelity ($\overline{\mathcal{F}}_{\mathrm{s}} = (2\mathcal{F}_{\mathrm{p}} + 1)/3$).

When the storage time between write and read is extended, the fidelity drops, as expected, reaching the above-mentioned classical threshold after ≥25 μs (Fig. 3d). We attribute this to residual, uncompensated magnetic fields, which lead to uncontrolled rotation of the atomic spin. By applying a magnetic guiding field of 44 mG along the quantization axis (Fig. 3e), the coherence time of the memory is significantly improved. While the fidelity of circularly polarized input states, which are stored in energy eigenstates of the atom, is constantly high over the tested time interval, the fidelity of linearly polarized input states shows the expected oscillation at twice the Larmor frequency of 62 kHz, with a decay time to the classical threshold of ≥170 μs. Cooling the atoms to their motional ground state, mapping the atomic states to a decoherence-protected basis during storage[8] and application of dynamical decoupling schemes[33] are possible means to further improve the coherence time.

For short storage times, a number of causes are expected to contribute to the deviation of the memory from perfect fidelity, one of them being erroneous initialization of the atomic state. However, part of the preparation errors are filtered out in the presented scheme as they will not lead to the emission of a herald photon. If one compares the fidelity of the memory with and without conditioning on the detection of a π-polarized herald photon, one finds that the conditioning improves the average state fidelity from

86.4 ± 0.1% to 94.7 ± 0.2% (Fig. 3b). This reveals another advantage of the herald photon in the presented memory scheme, namely its capability to detect and filter out certain errors during the storage process, leading to an improved fidelity. A further improvement of the fidelity can be achieved by disregarding photons that are emitted at a late stage of the readout process, leading to an average state fidelity reaching 97.7 ± 0.4%, at the cost of a reduced readout efficiency (Fig. 3c). The reason behind this is a finite probability for the atom to scatter a photon and return to the $F = 2$ hyperfine state prior to making the intended transition to the $F = 1$ hyperfine state, which could be further mitigated by a higher cooperativity of the qubit cavity.

To quantify the efficiency of the heralded memory, we define the single-photon heralding efficiency as the probability to detect a herald photon for a single photon sent onto the qubit cavity. For the presented memory, this efficiency is 11 ± 1%. It is reduced by a number of factors (see Methods), none of which is fundamental. The simplest way to improve the efficiency is to use state-of-the-art single-photon detectors, which would nearly double the heralding efficiency. Further improvements can be expected from an increased atom–photon coupling, which can be achieved by improving the localization of the atoms or by choosing different atomic states for performing the memory, such as having both the qubit and the herald cavity on the $F = 1 \leftrightarrow F' = 1$ transition of the D_2 line of ^{87}Rb.

The atomic states chosen here have the advantage that a successful readout process detunes the atom from the readout light, which allows for efficient readout of the qubit from the memory. We denote the readout efficiency as the probability for retrieving a photon in the fibre in front of the qubit cavity provided that the atom was transferred to the $F = 2$ state during the preceding write process. For the presented measurements, the readout efficiency was 56 ± 6% (see Methods for details).

For the measurements shown in Figs. 2 and 3, no elaborate pulse shaping was applied and the shapes of the pulses used during the write and read process result from the spectral response of acousto-optic modulators (which were used for switching the light) to rectangular electronic gate signals. The same measurements were carried out with more smoothly shaped laser pulses, without any significant difference in the performance of the memory (Supplementary Figs. 2 and 3). This illustrates the robustness of our memory scheme, which sets requirements on the impinging photons concerning their centre frequency and bandwidth, but functions completely independently of their temporal mode, which can be arbitrary and totally unknown. This feature can also be found in storage schemes based on the reflection of a photon from a cavity[9] as well as to some extent in ensemble-based memories, where it can be traded against multimode capacity[34], and constitutes a substantial practical advantage over memories based on stimulated Raman adiabatic passage in single emitters as well as ensemble-based memories with limited optical depth where control fields required during the storage process have to be adjusted to the arrival time as well as the amplitude and phase profile of the wavepackets of the incoming photons[6,35]. The bandwidth of the storage process of our memory results from an interplay of the different coupling and decay rates of the system. Based on the characterization of these rates and a simple, analytic model of the storage process (see Methods), we expect a bandwidth of 40 MHz. This is above the bandwidth of the acousto-optic modulators used for switching, thus explaining the vanishing effect of the different applied pulse shapes on the efficiency, and is in agreement with the absence of any visible additional distortion of the edges of the herald photons shown in Fig. 2 relative to the shape of the input pulses.

To determine the role of the vacuum field of the herald cavity in the emission of a herald photon, we carried out another series of measurements where the frequency of the herald cavity was

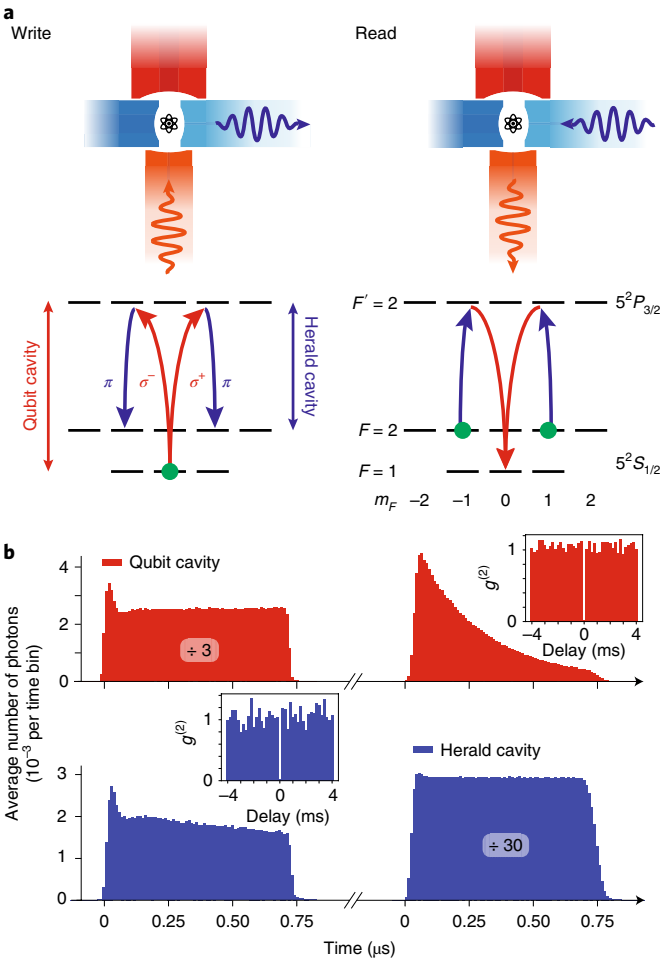

Fig. 2 | Scheme for the heralded quantum memory. a, Schematic of the storage scheme. The left side illustrates the write process, the right side the readout process. The upper part shows a drawing of the crossed cavities along with incoming and outgoing photons (wiggly arrows). The lower part shows the atomic-level scheme. Green circles indicate initial atomic populations and curved arrows show the transitions that occur during the write and readout process. **b**, Histograms of photons sent onto the cavities and leaving the cavities during the write process (left side) and the readout process (right side). The shown pulses sent onto the cavities were characterized during reference measurements with the cavities set out of resonance, when most of the light is directly reflected from the input mirrors of the cavities. Scaling factors indicate by how much the respective signals were reduced prior to plotting. The shape of a photon leaving a cavity reflects the shape of the coherent pulse sent onto the other cavity multiplied by the decaying probability for the atom to be still found in the initial state. The insets show $g^{(2)}$ correlation functions of herald photons (lower left) and the readout photons (upper right). The strong suppression of correlations at equal times is a signature of single photons.

detuned relative to the atomic $F = 2 \leftrightarrow F' = 2$ transition (Fig. 4a). The measurement results for both the single-photon storage efficiency and the single-photon heralding probability as a function of the herald cavity detuning are shown in Fig. 4b,c. The decrease of the transfer probability for increasing herald cavity detuning shows that qubit storage is predominantly induced by the vacuum field of the herald cavity. The process can be well described using a simple model, based on the generic situation of cavity quantum electrodynamics with a single atom coupled to the qubit cavity where the atom is subject to additional, Purcell-enhanced loss due to its

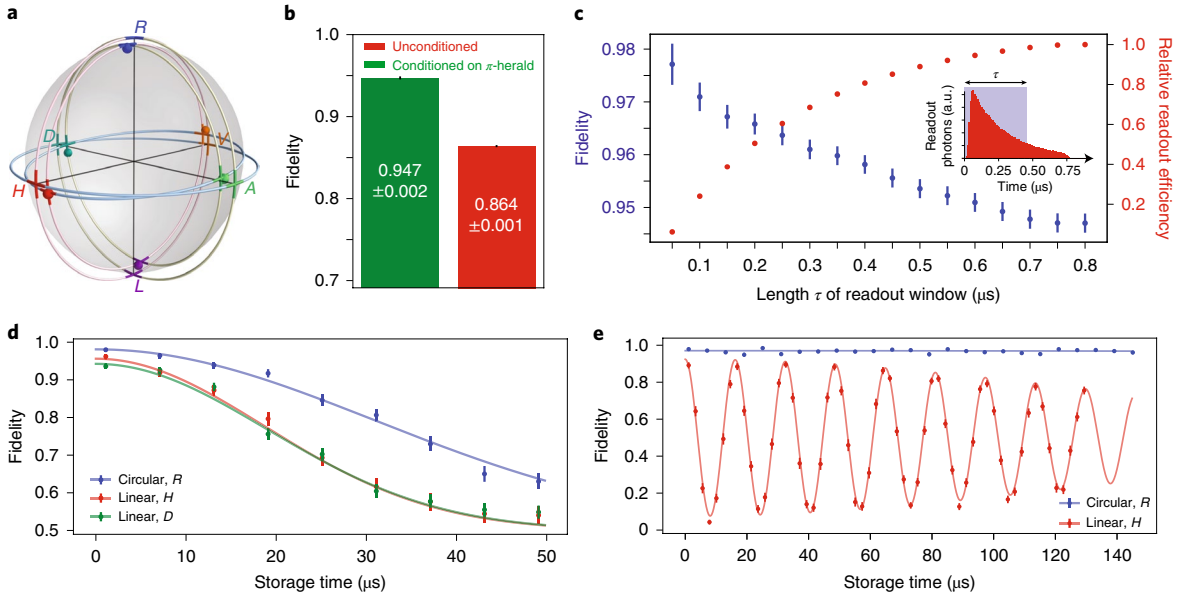

Fig. 3 | Fidelity of the heralded quantum memory. a, Poincaré sphere showing the quantum process underlying the memory for an effective storage time of 1.1 μs. It is reconstructed using a maximum-likelihood fit. The coloured spheres are the results of state tomography of the memory output for the correspondingly coloured and labelled input polarizations. The average state fidelity is 94.7 ± 0.2%. **b**, Average state fidelity of the readout photons with (green bar) and without (red bar) conditioning on the preceding detection of a herald photon, showing how the heralding improves the fidelity of the memory. **c**, Average state fidelity and relative readout efficiency for truncated readout photons. Disregarding late readout photons increases the fidelity due to a reduced probability for the atom to have scattered a photon prior to the emission of a photon into the qubit cavity. **d**, Fidelity of the memory for longer storage times without magnetic guiding field. The fidelity decays over time, reaching the classical limit at storage times ≥25 μs. **e**, Fidelity of the memory with an applied magnetic guiding field. While the fidelity of circular polarization input states stays constantly high over time, the fidelity for a linear input shows the expected oscillations, with an envelope reaching the classical limit at storage times ≥170 μs. Error bars in **b**–**e** indicate the 1σ confidence levels accounting for statistical uncertainties due to the finite number of detected photons.

coupling to the herald cavity (see Methods for details). Fit parameters of the model fitted to the single-photon storage efficiencies shown in Fig. 4b,c are heuristic factors, by which the atom–photon coupling rates of the two cavities deviate from their expected values (see Methods). We attribute these to imperfections in the localization of the atoms within the cavity modes and expect to be able to improve this in the future, for example by direct imaging of the atoms with a camera and subsequent feedback onto the atomic position. This holds potential for a further increase of the efficiency of the presented heralded quantum memory.

Although nodes operating with photons in the long-wavelength part of the optical spectrum can be directly used to operate short- to mid-distance networks such as those that connect several small quantum computing units to larger, more powerful clusters in a building or on a campus, long-distance fibre networks require photon transmission in one of the telecommunication bands to minimize losses during propagation. To that end, one might either place wavelength conversion units[36,37] between the nodes and the connecting quantum channels or implement nodes with quantum emitters that directly operate at a telecommunication wavelength. The latter can in fact be achieved with rubidium and a vacuum-stimulated Raman adiabatic passage involving higher-lying excited states of the atom[15].

Beyond telecommunication wavelengths, the large bandwidth of our system combined with photon-shape robustness might enable a memory for photons emitted by quantum dots[38], thereby promoting the development of hybrid quantum systems. Last, but not least, the two independently controllable crossed fibre cavities constitute a new platform for experiments on basic cavity quantum electrodynamics with two optical modes[39].

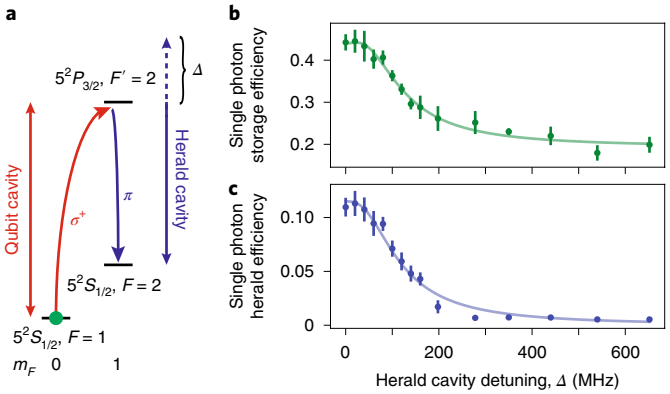

Fig. 4 | Heralded storage with variable herald cavity detuning. **a**, The heralded storage experiment was performed with variable detuning of the herald cavity, as indicated by the dashed arrow. The green circle indicates the initial atomic population and the curved arrows show the transitions that occur during the heralded storage process. **b**, The probability that a single photon sent onto the qubit cavity transfers the atom to the final $5^2S_{1/2}, F = 2$ state is shown for different herald cavity detunings. The decay of the storage efficiency with increasing herald cavity detuning shows that the storage process is induced by the vacuum field of the herald cavity. Error bars indicate the s.d. over all atoms contributing to the measurements. The solid line shows a simple model describing the storage process, fitted to the data (see Methods for details). **c**, Analogous to **b**, but showing the heralding efficiency for a single photon sent onto the qubit cavity. The detection efficiencies are included.

Online content

Any methods, additional references, Nature Research reporting summaries, source data, extended data, supplementary information, acknowledgements, peer review information; details of author contributions and competing interests; and statements of data and code availability are available at https://doi.org/10.1038/s41567-020-0855-3.

Received: 18 September 2019; Accepted: 17 February 2020;
Published online: 13 April 2020

References

1. Acín, A., Cirac, J. I. & Lewenstein, M. Entanglement percolation in quantum networks. *Nat. Phys.* **3**, 256–259 (2007).
2. Wehner, S., Elkouss, D. & Hanson, R. Quantum internet: a vision for the road ahead. *Science* **362**, eaam9288 (2018).
3. Ritter, S. et al. An elementary quantum network of single atoms in optical cavities. *Nature* **484**, 195–200 (2012).
4. Kimble, H. J. The quantum internet. *Nature* **453**, 1023–1030 (2008).
5. Reiserer, A. & Rempe, G. Cavity-based quantum networks with single atoms and optical photons. *Rev. Mod. Phys.* **87**, 1379–1418 (2015).
6. Gorshkov, A. V., André, A., Fleischhauer, M., Sørensen, A. S. & Lukin, M. D. Universal approach to optimal photon storage in atomic media. *Phys. Rev. Lett.* **98**, 123601 (2007).
7. Specht, H. P. et al. A single-atom quantum memory. *Nature* **473**, 190–193 (2011).
8. Körber, M. et al. Decoherence-protected memory for a single-photon qubit. *Nat. Photon.* **12**, 18–21 (2018).
9. Kalb, N., Reiserer, A., Ritter, S. & Rempe, G. Heralded storage of a photonic quantum bit in a single atom. *Phys. Rev. Lett.* **114**, 220501 (2015).
10. Reiserer, A., Kalb, N., Rempe, G. & Ritter, S. A quantum gate between a flying optical photon and a single trapped atom. *Nature* **508**, 237–240 (2014).
11. Tiecke, T. G. et al. Nanophotonic quantum phase switch with a single atom. *Nature* **508**, 241–244 (2014).
12. Shomroni, I. et al. All-optical routing of single photons by a one-atom switch controlled by a single photon. *Science* **345**, 903–906 (2014).
13. Scheucher, M., Hilico, A., Will, E., Volz, J. & Rauschenbeutel, A. Quantum optical circulator controlled by a single chirally coupled atom. *Science* **354**, 1577–1580 (2016).
14. Briegel, H.-J., Dür, W., Cirac, J. I. & Zoller, P. Quantum repeaters: the role of imperfect local operations in quantum communication. *Phys. Rev. Lett.* **81**, 5932–5935 (1998).
15. Uphoff, M., Brekenfeld, M., Rempe, G. & Ritter, S. An integrated quantum repeater at telecom wavelength with single atoms in optical fiber cavities. *Appl. Phys. B* **122**, 46 (2016).
16. Bussières, F. et al. Prospective applications of optical quantum memories. *J. Mod. Opt.* **60**, 1519–1537 (2013).
17. Hedges, M. P., Longdell, J. J., Li, Y. & Sellars, M. J. Efficient quantum memory for light. *Nature* **465**, 1052–1056 (2010).
18. Cho, Y.-W. et al. Highly efficient optical quantum memory with long coherence time in cold atoms. *Optica* **3**, 100–107 (2016).
19. Wang, Y. et al. Efficient quantum memory for single-photon polarization qubits. *Nat. Photon.* **13**, 346–351 (2019).
20. Borregaard, J., Kómár, P., Kessler, E., Sørensen, A. & Lukin, M. Heralded quantum gates with integrated error detection in optical cavities. *Phys. Rev. Lett.* **114**, 110502 (2015).
21. Lin, G. W., Zou, X. B., Lin, X. M. & Guo, G. C. Heralded quantum memory for single-photon polarization qubits. *EPL* **86**, 30006 (2009).
22. Koshino, K., Ishizaka, S. & Nakamura, Y. Deterministic photon–photon $\sqrt{\text{SWAP}}$ gate using a Λ system. *Phys. Rev. A* **82**, 010301 (2010).
23. Tanji, H., Ghosh, S., Simon, J., Bloom, B. & Vuletić, V. Heralded single-magnon quantum memory for photon polarization states. *Phys. Rev. Lett.* **103**, 043601 (2009).
24. Kurz, C. et al. Experimental protocol for high-fidelity heralded photon-to-atom quantum state transfer. *Nat. Commun.* **5**, 5527 (2014).
25. Yang, S. et al. High-fidelity transfer and storage of photon states in a single nuclear spin. *Nat. Photon.* **10**, 507–511 (2016).
26. Delteil, A., Sun, Z., Fält, S. & Imamoğlu, A. Realization of a cascaded quantum system: heralded absorption of a single photon qubit by a single-electron charged quantum dot. *Phys. Rev. Lett.* **118**, 177401 (2017).
27. Bechler, O. et al. A passive photon–atom qubit swap operation. *Nat. Phys.* **14**, 996–1000 (2018).
28. Chen, Y.-A. et al. Memory-built-in quantum teleportation with photonic and atomic qubits. *Nat. Phys.* **4**, 103–107 (2008).
29. Trautmann, N. & Alber, G. Dissipation-enabled efficient excitation transfer from a single photon to a single quantum emitter. *Phys. Rev. A* **93**, 053807 (2016).
30. Hunger, D. et al. A fiber Fabry–Perot cavity with high finesse. *New J. Phys.* **12**, 065038 (2010).
31. Uphoff, M., Brekenfeld, M., Rempe, G. & Ritter, S. Frequency splitting of polarization eigenmodes in microscopic Fabry–Perot cavities. *New J. Phys.* **17**, 013053 (2015).
32. Duan, L.-M. & Kimble, H. J. Scalable photonic quantum computation through cavity-assisted interactions. *Phys. Rev. Lett.* **92**, 127902 (2004).
33. Viola, L., Knill, E. & Lloyd, S. Dynamical decoupling of open quantum systems. *Phys. Rev. Lett.* **82**, 2417–2421 (1999).
34. Nunn, J. et al. Multimode memories in atomic ensembles. *Phys. Rev. Lett.* **101**, 260502 (2008).
35. Morin, O., Körber, M., Langenfeld, S. & Rempe, G. Deterministic shaping and reshaping of single-photon temporal wave functions. *Phys. Rev. Lett.* **123**, 133602 (2019).
36. Radnaev, A. G. et al. A quantum memory with telecom-wavelength conversion. *Nat. Phys.* **6**, 894–899 (2010).
37. Albrecht, B., Farrera, P., Fernandez-Gonzalvo, X., Cristiani, M. & de Riedmatten, H. A waveguide frequency converter connecting rubidium-based quantum memories to the telecom C-band. *Nat. Commun.* **5**, 3376 (2014).
38. Meyer, H. et al. Direct photonic coupling of a semiconductor quantum dot and a trapped ion. *Phys. Rev. Lett.* **114**, 123001 (2015).
39. Yoo, H. & Eberly, J. H. Dynamical theory of an atom with two or three levels interacting with quantized cavity fields. *Phys. Rep.* **118**, 239–337 (1985).

Methods

Crossed optical fibre cavities. At the heart of the experimental apparatus are two crossed optical fibre cavities, whose constituting mirrors were shaped on the end facets of optical fibres using CO_2 laser machining[30,31]. Each cavity consists of one highly reflective mirror and one outcoupling mirror. The outcoupling mirrors were shaped on the end facets of single-mode fibres (IVG Fiber, Cu800), while multimode fibres were used for the highly reflective mirrors (IVG Fiber, Cu50/200 and Cu50/125 for the qubit cavity and the herald cavity, respectively). CO_2 laser machining was performed using a CO_2 laser emitting at a wavelength of 9.3 μm. The laser beam was focused to the centre of the fibres with a beam waist of 120–400 μm. For the machining of the elliptical mirrors, a beam with an elliptical profile was used (ratio of the beam waists $w_y/w_x \approx 2.2$). The mirrors were shaped using 1 to 4 pulses with pulse lengths of 0.3–3.3 ms and a laser power of 50 W. The resulting radii of curvature of the fibre mirrors are 340 μm and 170 μm for the outcoupling and highly reflective mirror of the qubit cavity and $(R_x, R_y) = (100\,\mu\text{m}, 290\,\mu\text{m})$ and (90 μm, 230 μm) for the outcoupling and highly reflective mirror of the herald cavity, respectively. The exact values depend on the chosen region of interest as the mirror surfaces are not exactly spherical. The birefringent phase shift per roundtrip of the herald cavity that is expected due to the ellipticity of the mirrors[31] (1.7 mrad) is in good agreement with the direct measurement (1.8 mrad). The length of the qubit cavity and herald cavity are 162 μm and 80 μm, leading to expected mode waists at the cavity centre of $w = 6.5$ μm and $(w_x, w_y) = (3.5\,\mu\text{m}, 4.8\,\mu\text{m})$ for the qubit and herald cavity, respectively. The shaped fibre end facets are coated with dielectric mirror coatings (Laseroptik). The coating transmissions are 340 ppm for the outcoupling mirrors and 10 ppm for the highly reflective mirrors. Additional losses due to absorption, scattering and mode-coupling lead to finesses of $14,600 \pm 120$ and $15,680 \pm 30$ for the qubit and herald cavity, respectively. No decay of the finesse was observed over time. In combination with the cavity lengths, this corresponds to field decay rates of $2\pi \times 31.7$ MHz and $2\pi \times 59.8$ MHz for the qubit and herald cavity, respectively. The cavity fibres are mounted on stacks of piezo-electric slip-stick positioners that enable adjustment of the cavity lengths, mode matching between cavity mode and fibre mode at the outcoupling mirrors and overlap of the modes of the two cavities in vacuum. The overlap of the modes is aligned using cross-correlation of fluorescence photons scattered into the cavities by atoms falling through the cavities to a precision of ~1 μm.

Single atoms in crossed cavities. To bring a single atom into the cavities, we start by loading a cloud of ^{87}Rb atoms into a magneto-optical trap located ~10 mm above the cavities. After a trap loading phase (3 s), a short phase of molasses cooling is applied that cools the atoms to a temperature of ~16 μK before the atoms are released and begin to fall. Shortly afterwards, a red-detuned standing-wave optical dipole trap ($\lambda = 797.1$ nm) is switched on that guides the falling atoms towards the crossing point of the cavity modes. An additional cooling beam (lin ⊥ lin) that passes through the crossing point of the cavity modes under an oblique angle induces cooling forces that stop some of the atoms when they arrive in the cavities. The atoms are trapped in a 3D optical lattice ($U_0/k_B \approx 1$ mK) consisting of the above-mentioned red-detuned standing-wave trap and two blue-detuned intracavity dipole traps ($\lambda = 776.5$ nm and 774.6 nm). Light scattered into the cavities during cooling of the atoms is used to detect their presence inside the cavities. We use minimum bounds on the detected cooling light level to select atoms that are well placed within the cavity modes. Evaluation of $g^{(2)}$ correlation functions is used to ensure that only events where single atoms were trapped are considered for data analysis. The mean lifetime of atoms in the trap is typically on the order of 30 s.

Heralded storage with subsequent readout. The measurements for the experiments on heralded storage with subsequent readout were run with a repetition rate of 5 kHz (for tomography with short storage times) and 3.3 kHz (for characterization of the coherence times). Atom cooling for about 140 μs was followed by 45 μs of optical pumping to initialize the atom in the $|F = 1, m_F = 0\rangle$ state. To that end, light driving the $F = 2 \rightarrow F' = 2$ and $F = 2 \rightarrow F' = 3$ transitions was pumping atoms out of the $F = 2$ states (where the role of the light on the $F = 2 \rightarrow F' = 3$ transition was to break up dark states otherwise present among the $F = 2$ manifold), while the $F = 1 \rightarrow F' = 1$ transition was resonantly driven with π-polarized light below saturation to remove population from the $|F = 1, m_F = \pm 1\rangle$ states, leaving $|F = 1, m_F = 0\rangle$ as a dark state. To further reduce residual population in the $|F = 1, m_F = \pm 1\rangle$ states, the last 4 μs of optical pumping were done using π-polarized light resonant to the $F = 1 \rightarrow F' = 1$ transition only. This is expected to come at the cost of some additional population in the $F = 2$ states; however, that population does not emit any herald photons. Subsequently, a write pulse with variable polarization (duration $\tau \approx 740$ ns, average photon number $\overline{n} \approx 0.5$) was sent onto the qubit cavity. After a certain storage time, the atomic state was read out by sending a π-polarized read pulse ($\tau \approx 730$ ns, $\overline{n} \approx 6$) onto the herald cavity. The effective storage times were finely calibrated using the starting point of the oscillation of the memory fidelity for linearly polarized input states when a magnetic guiding field was applied along the axis of the qubit cavity. An additional short sequence of pumping the atom to $F = 1$ followed by a strong pulse ($\overline{n} \approx 10$) sent onto the qubit cavity had the main purpose of achieving $g^{(2)}$ correlation functions with higher signal-to-noise ratio to better discriminate between single and multiple trapped atoms, but was also used as a reference for efficiency calibration.

Polarization tomography set-ups that allowed for the polarization-resolved detection of light leaving the cavities or being reflected from their outcoupling mirrors were placed in front of both the qubit and the herald cavity. While the set-up in front of the herald cavity was mainly used to ensure that the herald photons were π-polarized, the set-up in front of the qubit cavity was used for full polarization tomography of the photons read out of the memory. Error bars and confidence intervals of the state fidelity $\mathcal{F}_s = \langle\psi_{in}|\rho_{out}|\psi_{in}\rangle$ of the memory output ρ_{out} with respect to the input state $|\psi_{in}\rangle$ account only for the statistical uncertainties of $p_{\parallel} = N_{\parallel}/(N_{\parallel} + N_{\perp})$ and follow the analysis of a Bernoulli process using normal approximation and 68% confidence levels. Here, $N_{\parallel}$ ($N_{\perp}$) is the number of counts detected with polarization parallel (orthogonal) to the input polarization. The stated uncertainty of the average state fidelity $\overline{\mathcal{F}_s}$ follows Gaussian uncertainty propagation. The process fidelity $\mathcal{F}_p$ is derived from a maximum-likelihood fit of a quantum process[7] to the set of photon counts $\{N_{ij} |\ i, j \in \{R, L, H, V, A, D\}\}$ acquired during the tomography measurements, where i refers to the input polarization and j to the detection basis. The uncertainty was assessed with a Monte Carlo method, using sets of numbers $\{\tilde{N}_{ij}\}$, where the $\tilde{N}_{ij}$ were randomly sampled from normal distributions centred at N_{ij} with standard deviation $\sqrt{N_{ij}}$. The standard deviation of the resulting $\{\tilde{\mathcal{F}}_p\}$ is used as the confidence interval for $\mathcal{F}_p$.

The probability $p_{H,1}$ to detect a herald photon for a single photon sent onto the qubit cavity was calculated from the probability $p_{H,\overline{n}}$ to detect a herald photon when a coherent laser pulse with $\overline{n}$ photons on average is sent onto the qubit cavity:

$$p_{H,1} = -\frac{p_{H,\overline{n}}}{\overline{n}} \frac{\ln(1 - p_{t,\overline{n}})}{p_{t,\overline{n}}} \tag{1}$$

where $p_{t,\overline{n}}$ is the probability to transfer the atom from the $F = 1$ to the $F = 2$ hyperfine ground state with the coherent pulse sent onto the qubit cavity. Equation (1) uses the Poissonian photon number statistics of the coherent input pulse and the fact that there is no dark state other than $F = 2$. The probability $p_{t,\overline{n}}$ was calculated from the ratio of herald counts detected during the write pulse divided by the number of counts detected during a much stronger reference pulse that to good approximation transferred all of the population. It can alternatively be assessed from a comparison of the probability to detect a photon during the readout process to the probability to detect a readout photon conditioned on a preceding herald event, which was used to check for consistency.

The heralding efficiency for the measurements with rectangular input pulses of 11 ± 1% is composed of 52 ± 3% single-photon transfer efficiency from the initial $F = 1$ state to the final $F = 2$ state, 79 ± 5% probability for emission of a π-polarized photon into the herald cavity during that process, 85 ± 1% probability for the photon to leave the cavity through the mirror leading to the detector, 80 ± 5% mode matching between the elliptical cavity mode and guided mode of the cavity fibre, 75 ± 5% transmission efficiency to the detector and 50 ± 4% detector efficiency.

The readout efficiency of 56 ± 6% is calculated from the probability to detect a readout photon subsequent to a heralded storage event. It consists of 92 ± 1% probability for the atom to be transferred to the $F = 1$ state, 86 ± 6% probability to emit a photon into the qubit cavity during that process, 79 ± 1% probability for the photon to leave the cavity through the right mirror and 90 ± 5% mode matching between cavity mode and fibre mode.

The stated uncertainties for the efficiencies and related parameters are estimated from the spread of parameters obtained for different measurements during the tomography and further account for systematic uncertainties of certain experimental parameters, like the input photon number and detector efficiencies, if relevant. The spread of evaluated parameters for different measurements is believed to mainly reflect the spread of trapping sites of atoms within the cavity modes, but can additionally be due to drifts of parameters, such as mode matchings, during the experiment.

Heralded storage for variable herald cavity detuning. The experimental sequence for measurements of heralded storage with variable detuning of the herald cavity was run at a repetition rate of 1 kHz and consisted of three subparts, each lasting for 300 μs. The first subpart started with 230 μs of cooling and optically pumping the atom to the $|5^2S_{1/2}, F = 1, m_F = 0\rangle$ state, before a weak coherent write pulse ($\overline{n} \approx 0.5$, circular polarization, duration ~800 ns) was sent onto the qubit cavity. Instead of subsequently mapping the atomic state back to a photon, cavity-assisted fluorescence state detection of the $|5^2S_{1/2}, F = 2\rangle$ state was carried out for ~60 μs. A short sequence of optically pumping the atom to the $|5^2S_{1/2}, F = 1\rangle$ hyperfine state was added at the end to discriminate single from multiple trapped atoms using $g^{(2)}$ correlation functions. The second and third subparts of the sequence were variants of the first and were used for reference. While the write pulse was replaced by a much stronger pulse ($\overline{n} \approx 50$) that transferred all the population to the $|5^2S_{1/2}, F = 2\rangle$ state in the second subpart, no pulse was sent onto the qubit cavity during the third subpart.

The probability $p_{t,\overline{n}}$ with which the atom is transferred from the $F = 1$ to the $F = 2$ hyperfine ground state when a coherent write pulse with $\overline{n}$ photons on

average is sent onto the qubit cavity was derived by comparing the state detection signals acquired during the three subparts of the experimental sequence, averaged over all sequences run on a given trapped atom. Alternatively, the ratio of herald photons detected during the regular write pulse and the strong reference pulse, as well as single-shot state detection, which was possible only for some herald cavity detunings, were used to check for consistency. Using the same assumptions as in equation (1), the single-photon storage efficiency p_s, that is, the probability for the atom to be transferred from the $F = 1$ to the $F = 2$ hyperfine state when a single photon is sent onto the qubit cavity, is derived from $p_{t,\overline{n}}$ as

$$p_s = -\frac{\ln(1 - p_t, \overline{n})}{\overline{n}}.$$

Single-photon heralding efficiencies were calculated using equation (1).

The data shown in Fig. 4 represent the average and standard deviation of the set of all contributing atoms for a given detuning Δ. The impact of different atoms was weighted by their storage time. Specifically, efficiencies were first calculated for all contributing atoms separately, yielding average values μ with statistical variance σ^2. These values were used to add as many normally distributed random numbers $X \approx \mathcal{N}(\mu, \sigma^2)$ to an overall set S_Δ as there were experimental sequences during the storage time of the atom. A Gaussian fit to S_Δ provided the efficiencies and standard deviations, as shown in Fig. 4.

Model for the vacuum-induced heralded storage. The model we use to describe the vacuum-induced storage process (as shown in Fig. 4) assumes operation of the herald cavity in the Purcell regime and is based on an evaluation of possible loss channels for a photon impinging onto the qubit cavity. One fraction of the photon, $\mathcal{P}_R$, will be back-reflected from the qubit cavity, another fraction, $\mathcal{P}_C$, will be lost from within the cavity due to scattering and absorption from the cavity mirrors and transmission through the mirror at the back of the cavity, and a third fraction, $\mathcal{P}_A$, will be scattered by the atom. This last fraction will go along with a transfer of the atom to the $F = 2$ hyperfine ground state with probability p_{F2}, leading to a storage efficiency p_s of

$$p_s(\gamma_P) = \mathcal{P}_A(\gamma_P) \times p_{F2}(\gamma_P) = (1 - \mathcal{P}_R(\gamma_P) - \mathcal{P}_C(\gamma_P)) \times \frac{\gamma/2 + \gamma_P}{\gamma + \gamma_P} \qquad (2)$$

where γ_P is the vacuum-induced decay rate into the herald cavity,

$$\gamma_P(\Delta_H) = \frac{g_H^2 \kappa_H}{\kappa_H^2 + (2\pi\Delta_H)^2}$$

which is a function of the detuning Δ_H between the atom and the herald cavity (Fig. 4a). Here, g_H and κ_H are the atom–cavity coupling rate and the field decay rate of the herald cavity, respectively.

The fractions $\mathcal{P}_R$ and $\mathcal{P}_C$ are deduced from the reflection and transmission coefficients of the qubit cavity, as calculated using the input–output formalism under the assumption of a weak cavity drive. The effect of the herald cavity enters via the Purcell-enhanced decay of the atom $\gamma \mapsto \tilde{\gamma} = \gamma + \gamma_p$. Denoting $\epsilon = (2\tilde{\gamma}\sqrt{\kappa_Q \kappa_{1Q}})/(g_Q^2 + \kappa_Q \tilde{\gamma})$, where g_Q and κ_Q are the atom–cavity coupling rate and the field decay rate of the qubit cavity, respectively, and κ_{1Q} is the decay rate through the outcoupling mirror, we obtain

$$\mathcal{P}_C = \frac{\kappa_Q - \kappa_{1Q}}{\kappa_Q} |\mu_{FC}|^2 |\epsilon|^2, \mathcal{P}_R = (1 - |\mu_{RC}|^2) + \left| \mu_{RC} - \mu_{FC} \sqrt{\frac{\kappa_{1Q}}{\kappa_Q}} \epsilon \right|^2. \qquad (3)$$

Here, μ_{FC} is the amplitude mode overlap between the mode of the qubit cavity and the guided mode of the fibre in front of it, and μ_{RC} is the amplitude mode overlap between the mode of the qubit cavity and the mode to which the incoming fibre mode is mapped when reflected off the curved outcoupling mirror of the qubit cavity.

The fit parameters of the model to the single-photon storage efficiencies shown in Fig. 4b are real mode overlaps μ_{FC} and μ_{RC} as well as heuristic factors by which the atom–cavity coupling rates are reduced compared to our expectations based on the cavity geometries. Their fitted values are 0.8 for μ_{FC} and μ_{RC}, and 0.5 and 0.6 for the reduction factors of the atom–cavity coupling rates of the qubit and herald cavity, respectively. The single-photon heralding probability, as shown in Fig. 4c, follows from equation (2) by assuming that only photons emitted during Purcell-enhanced decay are collected by the herald cavity. The only remaining free fit parameter in Fig. 4c is an overall detection efficiency for a photon present in the herald cavity ($\eta_{Det} = 0.3$); all other parameters used are from the fit of the single-photon storage efficiency (Fig. 4b).

Bandwidth of the storage process. To assess the bandwidth of the storage process of our memory, we use the same model as described in the previous section. This time, we consider the case where the impinging photon has a variable detuning Δ_{Ph} relative to the frequency of the qubit cavity and the atomic transition, while the herald cavity is kept on resonance. The loss fractions $\mathcal{P}_R(\Delta_{Ph})$ and $\mathcal{P}_C(\Delta_{Ph})$ are again calculated from the reflection and transmission coefficients of the qubit cavity[5] as given by the cavity input–output formalism, which results in a modification of the quantity ϵ used in equation (3), which is now given by

$$\epsilon(\Delta_{Ph}) = \frac{2\sqrt{\kappa_Q \kappa_{Q1}}(\tilde{\gamma} + 2\pi i \Delta_{Ph})}{g_Q^2 + (\kappa_Q + 2\pi i \Delta_{Ph})(\tilde{\gamma} + 2\pi i \Delta_{Ph})}.$$

Using this expression for ϵ in the expressions of equation (3), we calculate the heralding efficiency, η_{Herald}, as

$$\eta_{Herald}(\Delta_{Ph}) = (1 - \mathcal{P}_R(\Delta_{Ph}) - \mathcal{P}_C(\Delta_{Ph})) \times \frac{\gamma_P}{\tilde{\gamma}} \times \eta_{Det}$$

where η_{Det} is the detection efficiency for a photon present in the herald cavity. We calculate the bandwidth of the memory as the full-width at half-maximum of η_{Herald} as a function of the frequency detuning Δ_{Ph} of the input field. Using the same parameters as for the fitted model discussed in the previous section, we derive a bandwidth of our memory of ~40 MHz.

The duration of the shortest pulse that can still be stored with good efficiency is inversely proportional to the spectral bandwidth of the memory evaluated above. The factor of proportionality depends on the exact shape of the spectral response function and the temporal profile of the impinging photon (as well as obviously on the applied definition of spectral and temporal width) and is typically of the order 10^0.

Data availability

Source data for Figs. 1, 3 and 4 are provided with the paper. The data that support the findings of this study are available from the corresponding author upon reasonable request.

Acknowledgements

We thank S. Ritter and M. Uphoff for contributions during an early stage of this work and T. Urban for contributions to the design and fabrication of the experimental chamber. This work was supported by the Bundesministerium für Bildung und Forschung via the Verbund Q.Link.X (grant no. 16KIS0870), the Deutsche Forschungsgemeinschaft under Germany's Excellence Strategy (EXC-2111, 390814868) and the European Union's Horizon 2020 research and innovation programme via the project Quantum Internet Alliance (GA no. 820445). J.D.C. acknowledges support from the Alexander von Humboldt Foundation.

Author contributions

All authors contributed to the experiment, analysis of the results and writing of the manuscript.

Competing interests

The authors declare no competing interests.

Additional information

Supplementary information is available for this paper at https://doi.org/10.1038/s41567-020-0855-3.

Correspondence and requests for materials should be addressed to M.B.

Peer review information *Nature Physics* thanks Lijun Ma and the other, anonymous, reviewer(s) for their contribution to the peer review of this work.

Reprints and permissions information is available at www.nature.com/reprints.